Journal of Materials Chemistry C

ARTICLE

Temperature dependent piezoelectric response and strain-electric field hysteresis of rare-earth modified bismuth ferrite ceramics†

Received 00th May 2016,

DOI: 10.1039/x0xx00000x
www.rsc.org/

Julian Walker[a,b], Hana Ursic[b], Andreja Bencan[b], Barbara Malic[b], Hugh Simons[c], Ian Reaney[d], Giuseppe Viola[e], Valanoor Nagarajan[f], Tadej Rojac[b]

The rare-earth (RE)-modified bismuth ferrite (BiFeO3 or BFO) family of ferroelectrics have uncomplicated lead-free chemistries and simple perovskite structures. Due to the high Curie transition temperature of the parent $BiFeO_3$ perovskite (~830°C), they are promising piezoelectric materials for use at elevated temperatures. However, the influence of the specific RE species on the electromechanical behavior at high temperatures and above the coercive electric-field is not widely reported. Here, structural analysis over multiple length scales using X-ray diffraction, transmission electron microscopy and piezoresponse force microscopy is coupled with a high electric-field cycling study and *in-situ* converse d_{33} measurements up to 325°C for three RE-BFO ceramic compositions, $Bi_{0.86}Sm_{0.14}FeO_3$, $Bi_{0.88}Gd_{0.12}FeO_3$ and $Bi_{0.91}Dy_{0.09}FeO_3$. The ceramics exhibit different phase assemblages with varying amounts of polar rhombohedral *R3c* and intermediate antipolar orthorhombic *Pbam* phases as a function of the RE species. During electric-field cycling at electric-fields with amplitudes of 160 kV/cm, peak-to-peak strains of 0.23-0.27% are reached for all three compositions. However, there are qualitative differences in the field-induced strain and electric current behavior as a function of electric-field cycling and the materials exhibit an electrical-history dependent behavior. $Bi_{0.91}Dy_{0.09}FeO_3$ possesses an improved d_{33} stability as a function of temperature relative to the parent BFO perovskite and the highest depolarization temperature among the three RE-BFO compositions, with a stable d_{33} of ~22 pC/N up to 325°C.

I. Introduction

Rare-earth (RE) modified bismuth ferrites ($Bi_{1-x}RE_xFeO_3$, RE-BFO) capitalize on the unique properties of the parent bismuth ferrite (BFO): high remanent polarization (~90 μC/cm^2) [1, 2], multiferroic behavior [3] (Neel temperature T_N~370°C) and high ferroelectric-to-paraelectric transition temperature (T_c~830°C) [4]. The substitution of RE elements (e.g. La, Sm, Nd, Gd, Dy) for Bi^{3+} at the A-site of the BFO perovskite has a number of important consequences. It changes the antiferromagnetic response to ferromagnetic [5-7], improves the synthesis of ceramics by preventing SiO_2 impurities (existing as a common impurity of raw materials and airborne dust) from causing large amounts of undesirable secondary phases (e.g. $Bi_{25}FeO_{39}$) [8, 9] and, most importantly, enhances the electromechanical behavior [10, 11] - a highly sought after phenomenon in lead (Pb)-free piezoelectric materials [12, 13]. Their potential for enhanced piezoelectric activity and high temperature functionality make RE-BFO compositions attractive candidates for high-temperature piezoelectrics.

The prolific use of bulk piezoelectric ceramics for room temperature [14] and high-temperature [15-17] sensor and actuator devices means that material systems must be synthesized as polycrystalline ceramics if they are to have an appreciable technological impact. To date, preparing RE-BFO ceramics has proven to be arduous and the synthesis method has a significant impact on the chemical homogeneity, phase composition and functional behavior [18]. As a result, the reported electrical properties of RE-BFO ceramics vary widely [5, 9, 18-26], and a limited number of studies demonstrate either apparent saturated switching strains [9, 18], saturated polarizations [25, 26] or high depoling temperatures [26-28]. Therefore, further investigation is still required in order to characterize and understand the electromechanical properties and high-temperature functionality of RE-BFO ceramics.

Binary $BiFeO_3$–$REFeO_3$ phase diagrams proposed for RE-BFO ceramics [29] indicate that the RE species can influence two key aspects of the composition-structure relationship. First, the amount of an intermediate antipolar orthorhombic *Pbam* phase that coexists with the polar rhombohedral *R3c* phase, depends on both the RE content and RE species [29, 30]. Second, the RE species can also vary the curvature [31] of the phase boundary (i.e. the slope of the phase boundary in a temperature-composition phase diagram) between the polar rhombohedral *R3c* phase and the non-polar orthorhombic *Pnma* (or *Pbnm*) phase (referred to as a

[a] Materials Research Institute, Pennsylvania State University, University Park 16802, PA, USA.
[b] Electronic Ceramic Department, Jozef Stefan Institute, Jamova Cesta, Ljubljana 1000, Slovenia.
[c] Department of Physics, Technical university of Denmark, Lyngby DK-2800 kgs., Denmark.
[d] Department of Materials Science and Engineering, University of Sheffield, Mappin Street, Sheffield S1 3JD, United Kingdom.
[e] Department of Applied Scienc and Technology, Institute of Materials Physics and Engineering, Corso Duca degli Abruzzi 24, 10129 Torino, Italy.
[f] School of Materials Sceince and Engineering, University of New South Wales, NSW, Sydney, 2052, Australia.

† Electronic Supplementary Information (ESI) available: See DOI: 10.1039/x0xx00000x

morphotropic phase boundary (MPB) by Refs [10, 32, 33]). This suggests that each RE species has a different influence on the polar-to-non-polar phase transition temperature (i.e. T_c) for any given RE concentration.

RE-BFO epitaxial thin films, however, tell a different story. The RE substitution is considered universal (i.e. independent of the RE species) when the average atomic radius of the cations on the A-site (i.e. Bi and RE) is the same [11]. In these epitaxial thin film studies, the different species of RE does not have a significant influence on the structure or electromechanical properties when comparing compositions with the same average A-site ionic radius. This incongruity between the observations made on RE-BFO ceramics and epitaxial thin films may arise due to different factors which characterise the two material forms, such as chemical homogeneity, substrate effects in thin films and the complex elastic and electric boundary conditions of grains in a polycrystalline ceramic [34]. However, given the variability of the electrical behaviors and structures reported by the literature on RE-BFO ceramics [5, 9, 18-26], it is difficult to affirm whether or not the different RE species in concentrations corresponding to the same average A-site ionic radius have an appreciable influence on the phase composition and functional properties.

Depolarizing temperatures as high as ~650–700°C have recently been reported for RE-BFO ceramics co-substituted with two RE species (i.e. La and Sm) [27]. These high depolarization temperatures indicate a high T_c, and hence potential for these materials for applications at elevated temperatures. The high temperature functional potential and the unclear influence of different RE species in the chemical composition, mean that it is both timely and necessary to systematically evaluate the influence of the RE species on the phase assemblage and temperature dependence of the piezoelectric activity in comparable RE-BFO ceramics, i.e., compositions with the same average A-site ionic radii.

This work investigates the effects of the different RE species in RE-BFO compositions chosen so that the Bi/RE ratio produces ceramics with the same average A-site ionic radius. Compositions $Bi_{0.86}Sm_{0.14}FeO_3$, (14 mol% Sm, BSFO), $Bi_{0.88}Gd_{0.12}FeO_3$ (12 mol% Gd, BGFO) and $Bi_{0.91}Dy_{0.09}FeO_3$ (9 mol% Dy, BDFO) were prepared by a reproducible mechanochemical activation assisted synthesis technique that produces ceramics with a high level of chemical homogeneity (as reported in ref 18). Structural analysis over multiple length scales evaluates the variation in the domain structures and content of polar rhombohedral *R*3*c* to antipolar orthorhombic *Pbam* phases in each ceramic, shedding light on the link between the phase assemblage and the domain structure. A strain-electric-field cycling study highlights a strongly electric-field-history dependent ferroelectric-ferroelastic domain switching behavior across all three ceramics, revealing different evolutionary behaviors. Differential scanning calorimetry (DSC), dilatometry and measurements of the converse piezoelectric coefficient (d_{33}) as a function of temperature clarify the influence of the RE species on the temperature stability of the piezoelectric properties. The work thus provides valuable insight for identifying the RE species most appropriate for producing RE-BFO compositions with stable piezoelectric responses at elevated temperatures.

II. Experimental methods

A. Material synthesis

Ceramics were prepared via a mechanochemical activation assisted method in which milled and stoichiometric mixed powders Bi_2O_3 (99.998%, *Alfa Aesar*), Fe_2O_3 (99.999%, *Alfa Aesar*) and Sm_2O_3 (99.99%, *Metall*) underwent a total of 40 hours of high-energy ball milling in 180 ml WC-Co vials with 10 mm diameter WC-Co milling balls. The powder mixtures were reduced to approximately amorphous phases before being milled again in ethanol and dried for 12 h at 80°C (see ref [18] for further details). Dried powders were uniaxially pressed into pellets at 150 MPa and sintered for 3 h at 800°C for BSFO, BDFO and 820°C for BGFO.

B. Characterization of the structure, phase composition and domain structure

X-Ray Diffraction (XRD) patterns were recorded using a Panalytical X'Pert PRO diffractometer with a Cu source and $K_{\alpha 1}$ radiation (wavelength 1.54184 Å), measured in the 10–90° 2θ range, a step of 0.04° and an acquisition speed of ~1.5°/min. Structural quantification was performed via whole-pattern Rietveld refinement using the TOPAS R software package (Version 2.1, 2003, *Coelho* software). Two phases were used for structural fitting: (i) *R*3*c* phase (ICSD#15299) and (ii) *Pbam* phase (ICSD #160460). Analyses were conducted on crushed pellets.

Transmission Electron Microscopy (TEM) was performed with JEOL JEM 2010 equipped with a JEOL EDXS detector. The specimens were prepared by mechanical grinding, dimpling and final Ar-ion milling. The piezoresponse images were recorded with an atomic force microscope (AFM; Asylum Research, Molecular Force Probe 3D, Santa Barbara, CA, USA) equipped with a piezoresponse force (PFM) Dual AC Resonance Tracking mode. A tetrahedral Si tip coated with Ti/Ir was used with a radius of curvature ~20 nm on a Si cantilever coated with Ti/Ir (Asyelec, AtomicForce F&E GmbH, Mannheim, Germany). AC voltage in the range of 0–20 V was applied to the FM tip.

C. Electric-field cycling

Electric-field cycling was carried out to track the evolution of the strain-electric-field and current-electric-field hysteresis behavior from the virgin state of the material (never exposed to an electric-field prior to measurement) [35]. The change in the switching behavior as a function of the number of prior electric-field cycles evidences the electric-field history dependence. Measurements were made on ~0.2 mm thick samples with sputtered gold electrodes. An *axiACCT* TF 2000 analyzer with a *SIOS meßtechnik* laser interferometer and a *TREK* model 609E-6 (4 kV) high-voltage amplifier were used for measurements. Electric-fields with a maximum amplitude 160 kV/cm and driving electric-field frequency of 100 Hz were applied in a sinusoidal wave form. Peak-to-peak strains (S_{pp}) for asymmetric loops were determined as an absolute maximum value obtained by taking the difference between maximum and minimum values in strain-time plots.

D. High-temperature piezoelectric response and Curie transition

For d_{33} analysis samples were poled with a DC electric-field using a *Spellman* SL150 amplifier. Samples were submerged in a silicone-oil bath and kept at room temperature while the DC field was applied for 15 min at the maximum magnitudes of 140 kV/cm.

Converse piezoelectric measurements were performed using a custom-built set up consisting of a voltage function generator (SRS DS360) connected to a voltage amplifier (Trek 609E-6) for driving the samples, and a fiber-optic displacement sensor (*MTI* 2100 Fotonic Sensor) to measure piezoelectric displacements (for additional details see Ref.[36]). The measurements were carried out *in-situ* at elevated temperatures, with the sample maintained at elevated temperatures inside a furnace capable of 450˚C. A continuous bipolar sinusoidal electric-field of 10 Hz frequency and an amplitude of 2 kV/cm for RE-BFO and 1.8 kV/cm for BFO was applied at selected temperatures in the range 25˚C to 325˚C.

Depoling temperatures were measured *ex-situ*, meaning that the samples were annealed to the desired temperature and then cooled to room temperature before measuring the d_{33}. The d_{33} was determined at room temperature with a *Take Control*® piezometer system PM10 at ~200 Hz of driving stress frequency. The onset temperature of depoling was defined as the temperature at which the d_{33} first drops below its initial room temperature value.

DSC was conducted on a *Netzsch* thermogravimetric analyzer 400 series with a heating rate of 10°C/min. Dilatometry was conducted on sintered rectangular bars with dimensions 15.8 × 3 × 3 mm. An alumina tube furnace with *Netzsch* programming was used for heating with a rate of 2 °C/min up to 900°C. Both these analyses were performed with unpoled samples.

III. Results and discussion

A. Comparison of phase composition and domain structure

The concentrations of Sm, Gd and Dy in each composition $Bi_{0.86}Sm_{0.14}FeO_3$, (14 mol% Sm, BSFO), $Bi_{0.88}Gd_{0.12}FeO_3$ (12 mol% Gd, BGFO) and $Bi_{0.91}Dy_{0.09}FeO_3$ (9 mol% Dy, BDFO) respectively, were selected in order to result in an approximately equivalent average A-site ionic radius of ~1.35 Å, where the assumed ionic radii of each respective cation are r_{Sm}=1.28 Å, r_{Gd}=1.27 Å, r_{Dy}=1.24 Å and r_{Bi}=1.36 Å [37]. These compositions were used because they are expected to reside with similar proximity to the phase transition [11] between the polar rhombohedral *R*3*c* and non-polar orthorhombic *Pnma* [29] (or *Pbnm* [38]) phases (hereafter referred to as the polar-to-non-polar MPB). In RE-BFO systems, by increasing the concentration of RE in the perovskite, the intermediate antipolar orthorhombic *Pbam* phase [30] appears before the polar-to-non-polar MPB and coexists with the *R*3*c* phase [29], a phenomenon also recently observed in sol gel derived thin films [39]. In ceramics with optimized synthesis conditions (refer to Ref. 18), the *R*3*c* and *Pbam* phases exhibit nanoscale coexistence within the same grain and the BSFO structure closely resembles that observed in pulsed laser deposited epitaxial thin films [40].

Based on the powder XRD patterns of crushed pellets (**Fig. 1**), the structures of the three unpoled ceramics contain only *R*3*c* and *Pbam* phases. The *Pbam*:*R*3*c* phase-content ratio varies as a function of the RE species, in a similar fashion to previous reports for ceramics [19, 29]. Rietveld refinement of the XRD patterns indicates that the *Pbam* phase content in BSFO, BGFO and BDFO varies from ~60 wt%, ~10 wt% and <5 wt%, respectively (see supplementary for details). Despite a considerable overlap of the $(110)_{pc}$ Bragg peak (where *pc* denotes pseudo-cubic notation) from the *Pbam* and *R*3*c*

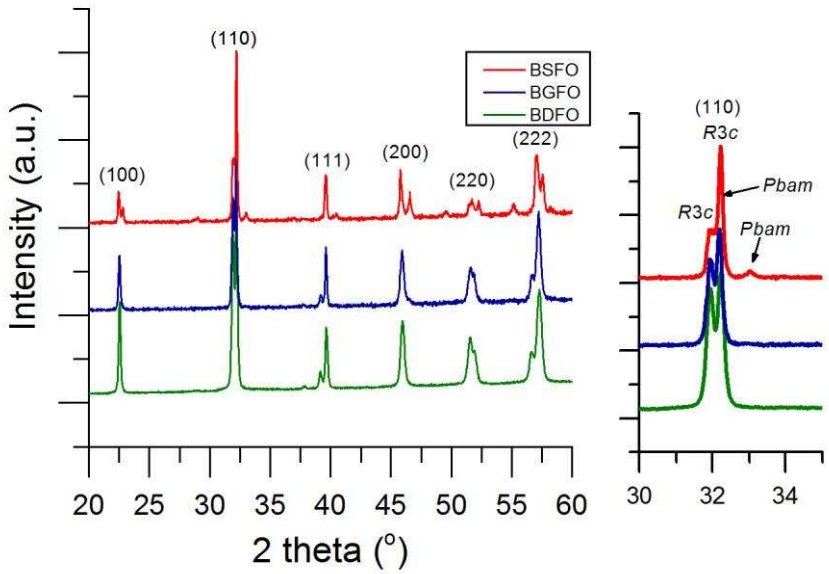

Figure 1. X-ray diffraction (XRD) pattern of BSFO (upper), BGFO (middle) and BDFO (lower). Main peaks marked with pseudo-cubic notation and peaks in the inset are labelled according to their associated phase i.e. *R*3*c* or *Pbam*.

phases, qualitative evidence of the changing *Pbam:R3c* phase-content ratio can be seen in the XRD patterns (**Fig. 1** inset).

HRTEM and PFM were employed to analyze the crystal structure, phase composition and domain structure of the ceramics at a local (nanometer and micrometer) level (**Fig. 2**). HRTEM images, with accompanying fast Fourier transforms (FFTs), generally agree with the XRD observations of phase coexistence. The BSFO ceramics (**Fig. 2a**) exhibit a nanoscale phase mixture of *R3c* and *Pbam*, highlighted by the FFTs (**Fig. 2a** inset). The BGFO ceramics also exhibit the coexistence of both *R3c* and *Pbam* phases (**Fig. 2c**), however, according to XRD the *Pbam* phase content is only ~ 10 wt% (see **Fig. 1**) and thus these regions are scarcer and were more difficult to find during HRTEM analysis. In the BDFO ceramics, the *Pbam* phase was not detected with HRTEM (**Fig. 2e**), although, according to XRD analysis, its presence cannot be completely ruled out due to the aforementioned XRD peak overlap.

The observed phase compositions are reflected in the domain structure of the accompanying PFM amplitude images (**Fig. 2b,d,f**). In BSFO, only some regions of the surface exhibited PFM contrast (**Fig. 2b**), with an irregular domain structure observed in small isolated regions. These regions with visible domains were previously identified as the *R3c* phase, and the regions exhibiting no PFM contrast (*i.e.* no visible domains) were identified as the *Pbam* phase [33, 41]. While PFM with its detection limitation (>40 nm) was unable to identify a domain structure in the *Pbam* phase, previous reports demonstrate that nanosized regions with greyscale contrast are visible with TEM, but are unidentified [33]. The BGFO domain structure reflects the reduced volume fraction of *Pbam* phase, exhibiting sub-micron sized irregular domains belonging to the *R3c* phase over the majority of the surface (**Fig. 2d**). Similarly, BDFO has domains belonging to the *R3c* phase throughout the majority of its surface (**Fig. 2f**) with both regular and irregular lamella-like sub-micron sized domains visible.

The different phase compositions and domain structures in the three ceramics may be related to their compositional proximity to the polar-to-non-polar MPB. For instance, in ferroelectrics such as $Pb(Zr,Ti)O_3$ (PZT), the domain structure changes markedly as the composition approaches the MPB [42, 43],

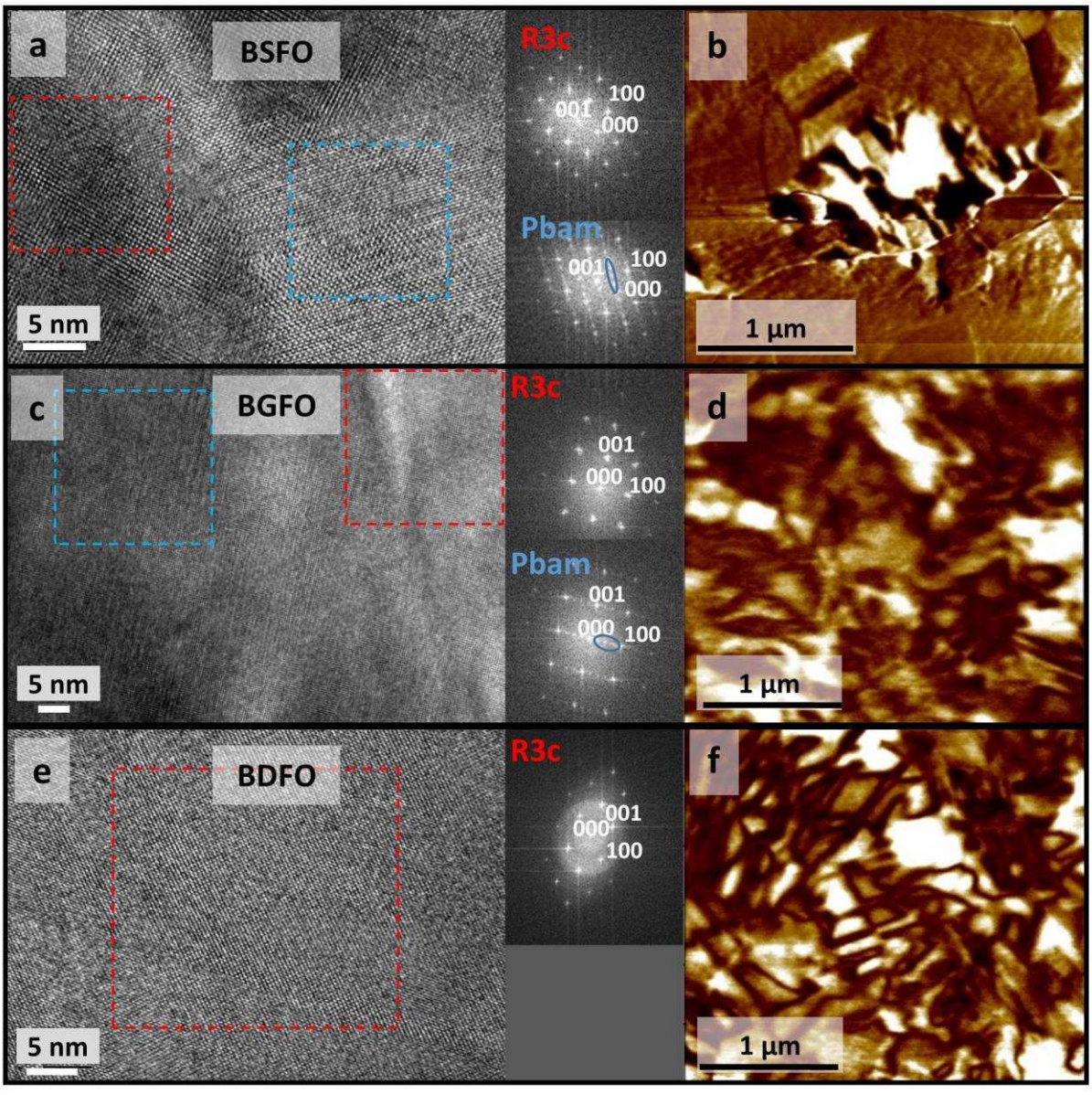

Figure 2 Local crystal structures and domains. Panels (a), (b) show the BSFO composition, (c), (d) BGFO and (e), (f) BDFO. (a), (c), (e) show high resolution transmission electron microscopy (HR-TEM) and insets of fast Fourier transforms (FFTs), taken from the structural regions marked with dashed squares in the corresponding HR-TEM images. Red squares for *R3c* and blue squares for *Pbam*. (b), (d), (f) show piezoresponse force microscopy (PFM) amplitude images.

and phase compositions in the vicinity of MPBs can also vary significantly as a result of two or more phases having a minimum barrier between their Gibbs free energies [44, 45]. The question still remains however, as to why a variation in the phase assemblages as a function of the RE species (in compositions with the same average A-site ionic radius) is not observed in RE-BFO epitaxial thin films [11]. One explanation may lie in the restriction of in-plane strain by the substrate in the epitaxial thin-film [46-48]. There are considerable differences in the lattice parameters of *R*3*c* and *Pbam* phases in RE-BFO compositions, discussed in detail by Levin *et* al., resulting in a difference of the unit cell volume < 1% [49]. Thus, for RE-BFO compositions with complex *R*3*c*-*Pbam* phase coexistence, the epitaxial stress of thin films could conceivably moderate the phase composition and create the incongruity observed between the phase assemblages in ceramics and epitaxial thin films with the same composition. In ceramics, the synthesis variables can also cause phase compositional differences, but this work utilized a consistent synthesis method that has previously been shown to produce highly reproducible ceramics with high chemical homogeneity and phase morphology similar to that of thin films [18]. The fluctuation in the phase composition in the three ceramics with different RE species is therefore unlikely to arise as a result of synthesis irregularities. The similar average grain-sizes among the ceramics (1-2 µm) also suggest that grain size effects are unlikely to explain the variation in domain structure observed. The role of the grain size in RE-BFO ceramic structure and electrical properties has not yet been reported in the literature and is thus an opportunity for future investigation.

B. Electric-field cycling behavior

For the electric-field cycling study, alternating (AC) electric-fields with amplitudes greater than the coercive field (E_c) were applied to virgin samples. This provides valuable information pertaining to the evolution of polarization and, in particular, strain [35]. Here the current-electric-field (*I*-*E*) and strain-electric-field (*S*-*E*) hysteresis are displayed in favour of polarization-electric-field (*P*-*E*) hysteresis (**Fig. 3**), as leakage current contributions can obscure critical *P*-*E* features such as remnant polarization [50]. Typical *P*-*E* loops can be found in the supplementary materials.

The *I*-*E* and *S*-*E* loops (**Fig. 3 a–c** and **3 d–f** respectively) show the behavior of each of the three compositions over the first ten cycles of electric-field with amplitude of 160 kV/cm and 100 Hz frequency. In all ceramics, an increase in the *I*-*E* peak is observed with each subsequent cycle, the largest increase occurs between the first and second cycles (**Fig. 3 a–c**, first loop shown in insets) and a difference in the peak intensities among the three RE-BFO compositions is observed after the first ten cycles (**Table 1**). The *S*-*E* hysteresis behavior of each composition shows an increase in the peak-to-peak strain (S_{pp}; determined as described in the experimental method) with each subsequent electric-field cycle (**Fig. 3 d–f**). The S_{pp} after ten electric-field cycles follows a similar trend to the current peak behavior as a function of RE-BFO composition (**Table 1**). This data gives a picture of the ceramic's "wake up" behavior [50, 51], that is, a progressive increase in the strain, current and polarization during switching-field cycling from the virgin state.

It is apparent from the *S*-*E* hysteresis behavior (**Fig. 3 d–f**), that the *S*-*E* loops abruptly develop an asymmetric shape after the first electric-field cycle, which becomes more pronounced with subsequent cycling. Such strain asymmetry is often symptomatic of ferroelectric fatigue [43,44]. All three RE-BFO compositions, however, are capable of producing *S*-*E* loops with greater symmetry when subjected to 10 kV/cm increments of the applied electric-field amplitude from zero to 180 kV/cm during their wake up (see supplementary material). Additionally, the virgin loop shape (first loop) can be approximately reproduced by annealing the already cycled samples above their T_c and again cycling them under electric-field (see supplementary material). This indicates that permanent mechanical damage during cycling (*e.g.,* cracking and/or microcracking) is unlikely to account for the asymmetrical S-E behavior, which may instead be due to the presence of an internal bias developing during the electrical cycles [52-55].

To further evaluate the differences in the electric-field cycling behavior of each composition, the maximum current density of each I-E loop is plotted against a logarithmic function of the number of cycles for the first 100 cycles (**Fig. 3g**). Similarly, the electric-field at which the maximum current occurs in the positive electric-field region (E_c^+) is plotted as a function of electric-field cycles in **Fig. 3h**. The BSFO composition shows a faster rate of current increase between the initial and final stages of cycling (see **Fig. 3g**). BGFO initially undergoes a rapid current density increase before slowing to a steady increase. In BDFO the current density steadily increases from the first cycle, showing a nearly linear relationship between current density and number of cycles in normal-log scale. Between the first and second electric-field cycles for all samples, the maximum current increases significantly and the E_c^+ reduces from the maximum field amplitude (160 kV/cm) in the first loop, to a value near ~130 kV/cm in the second loop (see **Fig 3h**). The E_c^+ reduces marginally (by ~5 kV/cm, or ~4%) for all compositions between the second and 100th cycle. Both *I*-*E* and *S*-*E* behavior indicate that there is likely an increased amount of ferroelectric-ferroelastic switching with each subsequent electric-

Table 1. Peak current and peak-to-peak strain values after the 1st and 10th consecutive electric-field cycles at an AC field magnitude of 160 kV/cm and frequency of 100 Hz for BSFO, BGFO and BDFO ceramics.

	BSFO		BGFO		BDFO	
cycle	**1st**	**10th**	**1st**	**10th**	**1st**	**10th**
Peak current density (A/m^2)	62	584	119	404	88	335
Peak-to-peak strain (%)	0.10	0.27	0.15	0.23	0.06	0.23

field cycle that continues over the first 100 electric-field cycles, reflecting a gradual wake up process.

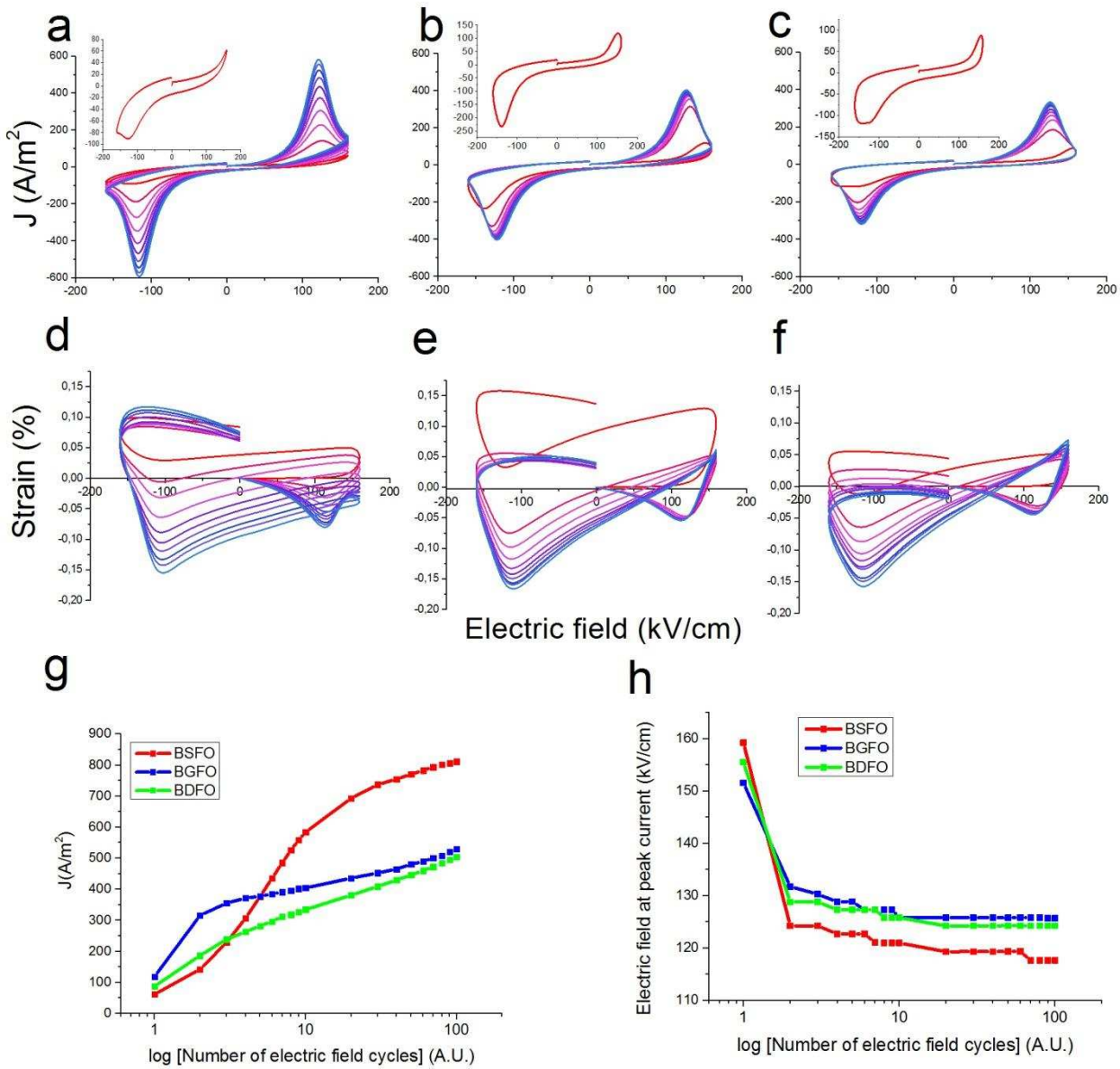

Figure 3 Electric-field cycling. (a), (b) and (c) show the current-electric-field hysteresis loops for the first 10 cycles of electric-field for BSFO, BGFO and BDFO respectively. Insets show the current loops from the virgin sample on first application of the electric field (first cycle). (d), (e), and (f) are the strain-electric-field hysteresis loops for the first ten cycles of electric field for the BSFO, BGFO and BDFO respectively. (g) shows the evolution of the maximum current as a function of the log of electric-field cycles 1 to 100, and (h) shows the electric-field at which the maximum current occurs also as a function of the log of electric-filed cycles 1 to 100 for each of the three compositions.

BFO-based materials can undergo electric-field induced phase transitions that may influence the electro-mechanical response [33, 56, 57]. In particular, an electric-field induced phase transition of *Pbam*-to-*R*3*c* phases was recently observed in BSFO composition close to the polar-to-non-polar MPB (i.e. 15.5mol% Sm) resulting in dual strain mechanisms [33]. This suggests that a similar transition may be expected in other RE-BFO compositions. The small amounts of *Pbam* phase present in the BGFO and BDFO ceramics, however, suggests that a *Pbam*-to-*R*3*c* phase transition may not significantly contribute to their strain behavior in these RE compositions. Moreover, the *Pbam*-to-*R*3*c* phase transition is particularly difficult to detect by XRD when there are only small amounts of *Pbam* phase present, due to the significant peak overlap of the *R*3*c* and *Pbam* patterns. Nevertheless, previous observations indicate that the *Pbam*-to-*R*3*c* phase transition in BSFO is slow (evolves over 100 or more electric-field cycles and is more apparent at low driving electric-field frequencies i.e. 0.1 Hz), meaning that if it contributes to the evolution of the *I-E* and *S-E*

loops in these RE-BFO compositions it is likely difficult to differentiate from other contributing phenomena. Additional factors that can influence the S-E hysteresis of RE-BFO may be, for example, the movement of pinning centers such as charged defects

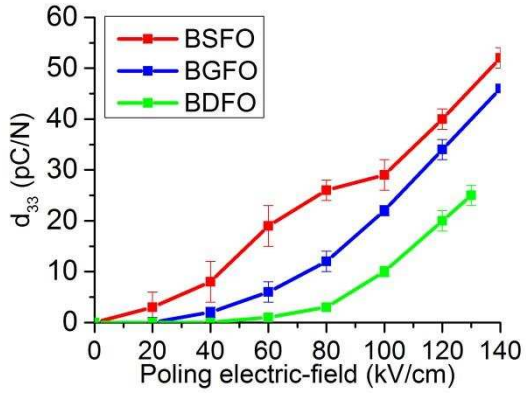

Figure 4 d_{33} as a function of the applied poling electric-field for each RE-BFO ceramic: BSFO (red), BGFO (blue) and BDFO (green). Error bars represent deviation of d_{33} value recorded with different samples and with multiple measurements on the same sample.

during electric-field cycling [58, 59], causing internal bias fields [52-55] that can influence strain.

C. High temperature piezoelectric functionality

The piezoelectric coefficient (d_{33}) of the three ceramics was first evaluated as a function of the poling-electric-field (**Fig. 4**). The maximum d_{33} values reached with ceramics poled by a DC electric-field are ~52 pC/N for BSFO, ~42 pC/N for BGFO and ~25 pC/N for BDFO. However, none of the ceramics were able to exhibit a saturation of the piezoelectric response at high poling fields before undergoing dielectric breakdown (see the increase of d_{33} as a function of poling-electric-field without a plateau towards the maximum field applied **Fig. 4**). Without first demonstrating a saturated polarization state, it is misleading to evaluate the d_{33} as a function of the RE species. All samples for which a d_{33} was measured (i.e. the study of *in-situ* d_{33} behavior and depoling temperature) were intentionally poled with electric-fields below the maximum poling-electric-field in order to preserve the integrity of the electrodes and the sample.

Using a custom-built experimental set-up to measure the *in-situ* converse d_{33} at elevated temperatures (consisting of an electric-field driving system, a fiber-optic sensor for mechanical displacement measurements and a furnace providing temperatures up to 400˚C; for details see experimental methods and ref [36]), a clear distinction in the temperature range of piezoelectric activity is observable between BSFO, BGFO, BDFO and BFO ceramics (**Fig. 5a**). (The BFO behaviour will be discussed later in text). Of BSFO, BGFO and BDFO ceramics, BDFO exhibits the most promising high-temperature capabilities with no deterioration of the d_{33} (~22 pC/N) up to a temperature of 325°C. The maximum measuring temperature of BDFO was not determined by the depoling of the material, but by the excessive electrical conductivity. This produced currents in excess of the current limit (20 mA) of the voltage amplifier, in turn preventing the driving of the sample at temperatures >325°C. With this operating temperature range and magnitude of d_{33}, BDFO is comparable to other lead-free compositions, such as $Bi_4Ti_3O_4$ (BiT) [60-62] and $BiFeO_3$–$BaTiO_3$–$Bi(Mg_{1/2}Ti_{1/2})O_3$ [63]. It must be mentioned, however, that the magnitude of the d_{33} response and even the temperature range of the BDFO composition, without further modification, is below that of some lead-containing candidate high-temperature compositions, such as $BiScO_3$-$PbTiO_3$ and $BiFeO_3$-$BiMgTiO_3$-$BiScO_3$-$PbTiO_3$ [64, 65]. In addition, the electrical conductivity of the BDFO at elevated temperatures would have to be further engineered before considering the materials for applications.

Figure 5 shows the results of four different measurements that explore the behavior of each composition as a function of temperature. These are *in-situ* d_{33}, depolarizing temperature determined with *ex-situ* d_{33} measurements, DSC and dilatometry. The *in-situ* measurement of d_{33} (**Fig. 5a**) shows an excellent correlation with the depoling temperature determined *ex-situ* for each composition (**Fig. 5b**), with the onset of depoling occurring at corresponding temperatures in both measurements for BSFO ~175°C and BGFO ~200°C ceramics. In the case of BDFO, an initial reduction of the d_{33} (*measured ex-situ*) is observed during the depoling measurements after 250°C, but rapid depoling is then not observed until after 350°C. During the *in-situ* measurement, the d_{33} of BDFO remains stable up to 325°C and thus the rapid decrease in d_{33} after 350°C is considered to result from depoling. Three vertical dashed lines marking the temperature of the onset of depoling are drawn across **Fig. 5 a–d** in order to highlight the correlation between the temperature dependent events observed with the four independent measurements.

In the DSC data two endothermic phenomena are visible for each BSFO, BGFO and BDFO compositions (**Fig. 5c**), similarly as that observed in Nd modified BFO compositions [67]. A small narrow endothermic trough occurs at approximately the same temperature in each composition (~360–370°C, indicated in **Fig. 5c** with a dashed box), and is identified as the ferromagnetic Curie transition temperature (often referred to as T_N due to the antiferromagnetic ordering of the parent BFO material). Another broader endothermic trough occurs at different temperatures for each of the three compositions. The onset of the broad troughs corresponds to the depoling temperatures of each respective composition and is thus considered to be related to the T_c (according to phase diagrams in Ref.[29]).

In the three ceramics, the dilatometry curves feature a local maxima and local minima in the temperature range 25°C–500°C (**Fig. 5d**). The temperature corresponding to the local maxima of the dilatometry curves is approximately 25°C below the onset of depoling temperature (**Fig. 5b**). After the local maxima the dilatometry curves show a relative shrinkage (ΔL/L) in the order of ~0.2–0.4% before reaching a local minimum, after which expansion occurs with increasing temperature. The local maxima and minima are located in the proximity of the T_c for each composition and they

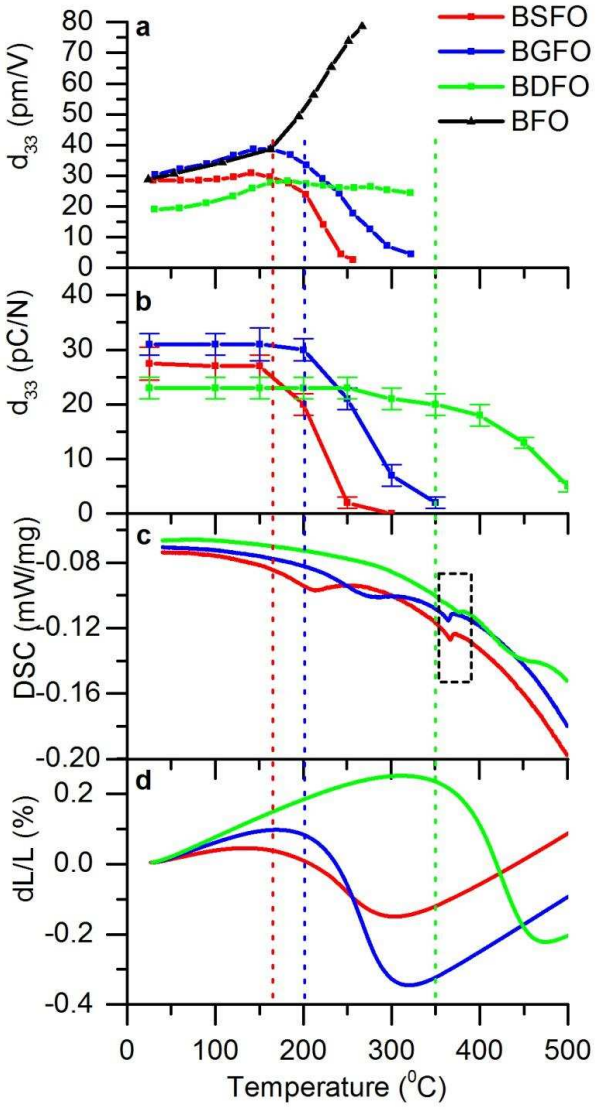

Figure 5 Temperature dependent properties of BSFO (red), BGFO (blue), BDFO (green) and BFO (black, only in a). (a) d_{33} measured *in-situ* at elevated temperatures. (b) the d_{33} measured *ex-situ* after annealing samples at the desired temperature and then cooling to room temperature. Error bars show the scatter of d_{33} values measured across the sample electrode. (c) differential scanning calorimetry (DSC) as a function of temperature. The dashed box denotes endothermic event associated with T_N. (d) dilatometry measured as a function of temperature. The vertical dashed lines for BSFO (red), BGFO (blue) and BDFO (green), mark the temperature of onset of depoling, that is the temperature at which the *ex-situ* measured d_{33} reduces to below the initial room temperature values for

result from the phase transition. At the T_c the phase changes from rhombohedral *R*3*c* to orthorhombic *Pbnm* in the BGFO and BDFO ceramics, and from a majority phase orthorhombic *Pbam* (with coexisting rhombohedral *R*3*c*) to orthorhombic *Pbnm* in BSFO (see **Fig. 1** and ref [11, 29, 49]). The phase transitions *R*3*c*-to-*Pbnm* and *Pbam*-to-*Pbnm* involve different rearrangements of the cation displacements, but have been shown to exhibit clear similarities, with similar contraction of the FeO_6 octahedral volume and corresponding reorientation of the oxygen octahedra, as well as similar abrupt changes of the unit cell volume < 1% [49]. This volume change is relatively large compared to other polar-to-non-polar transitions in ferroelectrics where the non-polar phase is cubic, for example in PZT a volume change around ~0.5% may be expected depending on the precise composition (i.e. Ti and Zr content) [66,67].

A smaller ΔL/L change is observed in BSFO relative to BGFO and BDFO, and the transition appears to be more diffuse as a function of temperature. We suggest that the BSFO dilatometry behavior may be related to the complex *R*3*c*-*Pbam* phase coexistence with high *Pbam* phase presence (~60 wt%) (see **Fig. 1** and **2**). Investigations by Kalantari *et* al. on Nb and Ti modified RE-BFO, with little or no *Pbam* phase, show that the dimensional changes measured by dilatometry are abrupt [68]. This supports the hypothesis that the *Pbam* phase may influence the kinetics of the phase transition at T_c and produce a small difference in the magnitude of the dimensional change.

Despite their approximately equivalent average A-site atomic radii, it is apparent that the onset temperatures for depoling of these RE-BFO ceramics are different and spread over a temperature range of approximately 175–325°C. Compositional factors may influence the temperature of this polar-to-non-polar phase transition at T_c, *i.e.* the RE species and the molar percentage of RE present. T_c was shown to congruently change with the polarizability of the RE species despite a moderate scatter of the data [29]. This implicates the polarizability of the RE species as a possible influence to the T_c, but does not explain why the same transition temperature variation has not been reported for RE-BFO epitaxial thin films, increasing the complexity of the problem.

The temperature dependent d_{33} behavior of BFO is also given together with BSFO, BGFO and BDFO in **Fig. 5a**, in order to provide insight into the influence of RE substitution on BFO. During the *in-situ* measurement of d_{33} as a function of temperature, BSFO and BGFO experience a decline of the d_{33} due to depoling in the vicinity of their respective T_c (also evident in **Fig. 5b**). However, the T_c of BDFO (325˚C) and BFO (830˚C [4]) are both above the test temperature range (25-300 ˚C) and neither experience a significant decrease of d_{33} due to depoling during the *in-situ* measurement. In this temperature range (i.e. 25–300°C), BDFO clearly exhibits less variation of d_{33} as a function of temperature relative to BFO. This is exemplified by the maximum d_{33} value at elevated temperatures calculated as a percentage of the room temperature d_{33} for each ceramics, and is ~30% for BDFO and ~170% for BFO.

The improved stability of the d_{33} of BDFO relative to BFO as a function of temperature, may have multiple origins. For example, differences in the thermally activated domain-wall mobility [69], and piezoelectric Maxwell-Wagner (M-W) behavior [36]. In BFO, the local conductivity at conductive domain walls (DW) and grain boundaries was found to affect the macroscopic d_{33} response through linear and non-linear piezoelectric Maxwell-Wagner

mechanisms. This was suggested in BFO ceramics based on combined analysis of the macroscopic piezoelectric response as a function of frequency and amplitude of the driving electric field (measured at room temperature) and of the local conductivity probed by atomic-force microscopy (c-AFM) analysis. As it is known that DW motion can have a dominant effect on the weak field dielectric and piezoelectric properties, contributing to as much as 70% of the total macroscopic response in ferroelectric materials [70, 71], and the DW conductivity can influence the DW dynamics [36], it is then conceivable that the DW conductivity may play a role in the temperature dependence of the macroscopic d_{33}. We thus propose that the improved d_{33} temperature stability of BDFO ceramics relative to BFO at elevated temperatures below the T_c, may arise from BDFO having different nanoscale properties to BFO, for example, reduced local conductivities at domain walls and grain boundaries.

IV. Summary and conclusion

The three RE-BFO compositions demonstrate clear distinctions in their quantitative phase composition, domain structure and temperature dependent piezoelectric activity despite an equivalent average A-site atomic radius. The ceramics exhibited coexistence of a polar rhombohedral *R3c* and anti-polar orthorhombic *Pbam* phase, with a *Pbam* content estimated from X-Ray diffraction analysis as ~60 wt%, ~10 wt% and <5 wt% for BSFO, BGFO and BDFO ceramics, respectively. The high-resolution TEM studies confirmed the simultaneous presence of both phases at the nanoscale. By using piezoresponse force microscopy, the presence of domains was found in the regions where the *R3c* phase was dominant, while no domains could be detected in the *Pbam* phase regions. All three compositions exhibit a response to electric field cycles, characterized by a gradual wake up behavior and progressive evolution towards an asymmetric strain-electric-field hysteresis response. One likely contributing factor to the wake up feature is the electric-field induced transition of *Pbam-to-R3c* phase, but as the extent *Pbam* phase varies with the type of RE species other phenomena are likely to be involved. The asymmetry in the strain-electric-field curves suggests that one such phenomenon is a biasing effect of as yet unknown type and origin that may develop during the electrical cycles and influence the ferroelectric/ferroelastic domain switching process. The thermal depoling studies are in good agreement with thermal analysis data regarding the onset and the evolution of the depolarization process. The BDFO ceramic provide a more stable d_{33}, relative to BFO, as a function of temperature in the range 25°C to 350°C, and exhibits the highest T_c of the three RE-BFO compositions.

Acknowledgements

This work was jointly funded by *Slovenian Research Agency program "Electronic Ceramics, Nano, 2D and 3D Structures" (P2-0105)*, project grant *"High-Performance Piezoelectric Materials for Sensors and Actuators in High-Temperature Applications" (J2-5483)*, *Australian Research Council (ARC) grant LP 0991794* together with *Thales Australia (under the advisement of Valsala Kurusingal and Peter Bryant)*. HS acknowledges support from the Danish Research Foundation FTP individual postdoctoral grant.

References

1. J. Wang, J. B. Neaton, H. Zheng, V. Nagarajan, S. B. Ogale, B. Liu, D. Viehland, V. Vaithyanathan, D. G. Schlom, U. V. Waghmare, N. A. Spaldin, K. M. Rabe, M. Wuttig and R. Ramesh, *Science*, 2003, **299**, 1719-1722.
2. D. Lebeugle, D. Colson, A. Forget and M. Viret, *Appl. Phys. Lett.*, 2007, **91**, 022907.
3. C. Tabares-Muñoz, J. P. Rivera, A. Bezinges, A. Monnier and H. Schmid, *Jap. J. Appl. Phys.*, 1985, **24**, 1051.
4. J. M. Moreau, C. Michel, R. Gerson and W. J. James, *J. Phys. Chem. Solids*, 1971, **32**, 1315-1320.
5. G. L. Yuan and S. W. Or, *J. Appl. Phys.*, 2006, **100**, 5.
6. V. A. Khomchenko, D. A. Kiselev, I. K. Bdikin, V. V. Shvartsman, P. Borisov, W. Kleemann, J. M. Vieira and A. L. Kholkin, *Appl. Phys. Lett.*, 2008, **93**, 3.
7. M. Deepam, T. Harikishan, G. Ashish, P. Brajesh, C. Prem and H. C. Verma, *J. Phys. Condens. Matter*, 2009, **21**, 026007.
8. M. Valant, A.-K. Axelsson and N. Alford, *Chem. Mater.*, 2007, **19**, 5431-5436.
9. J. Walker, B. Budic, P. Bryant, V. Kurusingal, C. C. Sorrell, A. Bencan, T. Rojac and V. Nagarajan, *IEEE Trans. on UFFC*, 2015, **62**, 83-87.
10. S. Fujino, M. Murakami, V. Anbusathaiah, S. H. Lim, V. Nagarajan, C. J. Fennie, M. Wuttig, L. Salamanca-Riba and I. Takeuchi, *Appl. Phys. Lett.*, 2008, **92**, 202904.
11. D. Kan, L. Pálová, V. Anbusathaiah, C. J. Cheng, S. Fujino, V. Nagarajan, K. M. Rabe and I. Takeuchi, *Adv. Funct. Mater.*, 2010, **20**, 1108-1115.
12. Y. Saito, H. Takao, T. Tani, T. Nonoyama, K. Takatori, T. Homma, T. Nagaya and M. Nakamura, *Nature*, 2004, **432**, 84-87.
13. E. Cross, *Nature*, 2004, **432**, 24-25.
14. K. Uchino, *Piezoelectric actuators and ultrasonic motors*, Kluwer accademic publishers, USA, 1996.
15. T. Stevenson, D. G. Martin, P. I. Cowin, A. Blumfield, A. J. Bell, T. P. Comyn and P. M. Weaver, *J. Mater. Sci. Mater. Electron*, 2015, **26**, 9256-9267.
16. R. C. Turner, P. A. Fuierer, R. E. Newnham and T. R. Shrout, *Appl. Acoust.*, 1994, **41**, 299-324.
17. D. Damjanovic, *Curr. Opin. Solid State Mater. Sci.*, 1998, **3**, 469-473.
18. J. Walker, P. Bryant, V. Kurusingal, C. Sorrell, D. Kuscer, G. Drazic, A. Bencan, V. Nagarajan and T. Rojac, *Acta Mater.*, 2015, **83**, 149-159.
19. I. O. Troyanchuk, D. V. Karpinsky, M. V. Bushinsky, O. S. Mantytskaya, N. V. Tereshko and V. N. Shut, *J. Am. Ceram. Soc.*, 2011, **94**, 4502-4506.
20. G. L. Yuan and S. W. Or, *Appl. Phys. Lett.*, 2006, **88**, 062905.
21. V. A. Khomchenko, J. A. Paixao, B. F. O. Costa, D. V. Karpinsky, A. L. Kholkin, I. O. Troyanchuk, V. V.

Shvartsman, P. Borisov and W. Kleemann, *Cryst. Res. Technol.* , 2011, **46**, 238-242.

22. Y. Yao, W. Liu, Y. Chan, C. Leung, C. Mak and B. Ploss, *Int. J. Appl. Ceram. Tech*, 2010, **8**, 1246-1253.
23. Y. B. Yao, W. C. Liu and C. L. Mak, *J. Alloys Compd.*, 2012, **527**, 157-162.
24. V. Koval, I. Skorvanek, M. Reece, L. Mitoseriu and H. Yan, *J. Euro. Ceram. Soc.*, 2014, **34**, 641-651.
25. S. Zhang, L. Wang, Y. Chen, D. Wang, Y. Yao and Y. Ma, *J. Appl. Phys.*, 2012, **111**, 4105-4109.
26. X. Chen, Y. Wang, Y. Yang, G. Yuan, J. Yin and Z. Liu, *Solid State Commun.*, 2012, **152**, 497-500.
27. T. Zheng and J. Wu, *J. Mater. Chem. C*, 2015, **3**, 3684-3693.
28. T. Zheng and J. Wu, *J. Mater. Chem. C*, 2015, **3**, 11326-11334.
29. S. Karimi, I. M. Reaney, Y. Han, J. Pokorny and I. Sterianou, *J. Mater. Sci.*, 2009, **44**, 11.
30. S. Karimi, I. M. Reaney, I. Levin and I. Sterianou, *Appl. Phys. Lett.*, 2009, **94**, 3.
31. S. Zhang and T. R. Shrout, *IEEE trans. Ultra. Ferro. Freq. contol.*, 2010, **57**, 2138-2146.
32. A. Y. Borisevich, E. A. Eliseev, A. N. Morozovska, C. J. Cheng, J. Y. Lin, Y. H. Chu, D. Kan, I. Takeuchi, V. Nagarajan and S. V. Kalinin, *Nature Commun.*, 2012, **3**, 775.
33. J. Walker, H. Simons, D. O. Alikin, A. P. Turygin, V. Y. Shur, A. L. Kholkin, H. Ursic, A. Bencan, B. Malic, V. Nagarajan and T. Rojac, *Sci. Rep.*, 2016, **6**, 19630.
34. D. Damjanovic, *Rep. Prog. Phys.*, 1998, **61**, 1267-1324.
35. G. Viola, T. Saunders, X. Wei, K. B. Chong, H. Luo, M. J. Reece and H. Yan, *J. Adv. Dielectr.* 2013, **03**, 1350007.
36. T. Rojac, H. Ursic, A. Bencan, B. Malic and D. Damjanovic, *Adv. Funct. Mater.*, 2015, **25**, 2099-2108.
37. R. D. Shannon, *Acta Cryst*, 1976, **A32**, 751.
38. M. Kubota, K. Oka, Y. Nakamura, H. Yabuta, K. Miura, Y. Shimakawa and M. Azuma, *Jap. J. Appl. Phys*, 2011, **50**, 09NE08.
39. W. Sun, J.-F. Li, Q. Yu, L.-Q. C, J. Mater. Chem. C, 2015, **3**, 2115-2122.
40. C. J. Cheng, A. Y. Borisevich, D. Kan, I. Takeuchi and V. Nagarajan, *Chem. Mater.*, 2010, **22**, 2588-2596.
41. D. O. Alikin, A. P. Turygin, J. Walker, T. Rojac, V. V. Shvartsman, V. Y. Shur and A. L. Kholkin, *J. Appl. Phys.*, 2015, **118**, 072004.
42. T. Asada and Y. Koyama, *Phys. Rev. B*, 2007, **75**, 214111.
43. D. I. Woodward, J. Knudsen and I. M. Reaney, *Phys. Rev. B*, 2005, **72**, 104110.
44. W. Cao and L. E. Cross, *Jap. J. Appl. Phys.*, 1992, **31**, 1399.
45. W. Cao and L. E. Cross, *J. Appl. Phys.*, 1993, **73**, 3250-3255.
46. N. setter, D. Damjanovic, L. Eng, G. Fox, S. Gevorgian, S. Hong, A. Kingon, H. Kohlstedt, N. Y. Park, G. B. Stephenson, I. Stolitchnov, A. K. Taganstev, D. V. Taylor, T. Yamada and S. Steriffer, *J. Appl. Phys.*, 2006, **100**, 46.
47. H. J. Kim, S. H. Oh and H. M. Jang, *Appl. Phys. Lett.*, 1999, **75**, 3195-3197.
48. E. Suhir, *J. Appl. Mech.*, 1988, **55**, 143-148.
49. I. Levin, S. Karimi, V. Provenzano, C. L. Dennis, H. Wu, T. P. Comyn, T. J. Stevenson, R. I. Smith and I. M. Reaney, *Phys. Rev. B*, 2010, **81**, 020103.
50. T. Schenk, E. Yurchuk, S. Mueller, U. Schroeder, S. Starschich, U. Böttger and T. Mikolajick, *Appl. Phys. Rev.*, 2014, **1**, 041103.
51. N. Menou, C. Muller, I. S. Baturin, V. Y. Shur and J.-L. Hodeau, *J. Appl. Phys.*, 2005, **97**, 064108.
52. T. Schenk, M. Hoffmann, J. Ocker, M. Pešić, T. Mikolajick and U. Schroeder, *ACS Appl. Mater. Inter.*, 2015, **7**, 20224-20233.
53. X. Ren, *Nature Mater.*, 2004, **3**, 4.
54. G. Arlt and H. Neumann, *Ferroelectrics*, 1988, **87**, 109-120.
55. M. Ozgul, S. Trolier-Mckinstry and C. Randall, *J. Electroceram.*, 2008, **20**, 317-318.
56. R. J. Zeches, M. D. Rossell, J. X. Zhang, A. J. Hatt, Q. He, C.-H. Yang, A. Kumar, C. H. Wang, A. Melville, C. Adamo, G. Sheng, Y.-H. Chu, J. F. Ihlefeld, R. Erni, C. Ederer, V. Gopalan, L. Q. Chen, D. G. Schlom, N. A. Spaldin, L. W. Martin and R. Ramesh, *Science*, 2009, **326**, 977-980.
57. J. X. Zhang, XiangB, HeQ, SeidelJ, R. J. Zeches, YuP, S. Y. Yang, C. H. Wang, Y. H. Chu, L. W. Martin, A. M. Minor and R. Ramesh, *Nature Nano*, 2011, **6**, 98-102.
58. M. I. Morozov and D. Damjanovic, *J. Appl. Phys.*, 2010, **107**, 034106.
59. T. Rojac, M. Kosec, B. Budic, N. Setter and D. Damjanovic, *J. Appl. Phys.*, 2010, **108**, 074107.
60. M. Villegas, A. C. Caballero, T. Jardiel, C. Aragó, J. Maudes and I. Caro, *Ferroelectrics*, 2009, **393**, 44-53.
61. H. Nagata, T. Tokutsu, D. Nakai, Y. Hiruma and T. Takenaka, *Ferroelectrics*, 2008, **368**, 202-208.
62. S. H. Hong, S. Trolier-McKinstry and G. L. Messing, *J. Am. Ceram. Soc.*, 2000, **83**, 113-118.
63. C. Zhou, A. Feteira, X. Shan, H. Yang, Q. Zhou, J. Cheng, W. Li and H. Wang, *Applied Physics Letters*, 2012, **101**, 032901.
64. R. E. Eitel, C. A. Randall, T. R. Shrout, P. W. Rehrig, W. Hackenberger and S. E. Park, *Jap. J. Appl. Phys.,* 2001, **40**, 5999-6002.
65. S. Tae-Ho, E. E. Richard, R. S. Thomas, A. R. Clive and H. Wes, *Jap. J. Appl. Phys.*, 2003, **42**, 5181.
66. B. Jaffe, W. R. J. Cook and H. Jaffe, eds., *Piezoelectric Ceramics*, Accademic Press Inc. London Ltd., London, 1971.
67. X. Dai, Z. Xu and D. Viehland, *J. Am. Ceram. Soc.*, 1995, **78**, 2815-2827.
68. K. Kalantari, I. Sterianou, D. C. Sinclair, P. A. Bingham, J. Pokorny and I. M. Reaney, *J. Appl. Phys.*, 2012, **111**, 064107.
69. X. L. Zhang, Z. X. Chen, L. E. Cross and W. A. Schulze, J. Mater. Sci., 1983, **18**, 968-972.

70. E. I. Bondarenko, V. Y. Topolov and A. V. Turik, *Ferroelect. Lett.,* 1991, **13**, 13-19.
71. G. Arlt and N. A. Pertsev, *J. Appl. Phys.*, 1991, **70**, 2283-2289.

